

Partial volume estimation in brain MRI revisited

Alexis Roche^{1,2,3} and Florence Forbes⁴
for the Alzheimer’s Disease Neuroimaging Initiative**

¹ Siemens Advanced Clinical Imaging Technology, Lausanne, Switzerland

² Department of Radiology, CHUV, Lausanne, Switzerland

³ Signal Processing Laboratory (LTS5), EPFL, Lausanne, Switzerland

⁴ Mistis Project, INRIA, Grenoble, France

Abstract. We propose a fast algorithm to estimate brain tissue concentrations from conventional T1-weighted images based on a Bayesian maximum a posteriori formulation that extends the “mixel” model developed in the 90’s. A key observation is the necessity to incorporate additional prior constraints to the “mixel” model for the estimation of plausible concentration maps. Experiments on the ADNI standardized dataset show that global and local brain atrophy measures from the proposed algorithm yield enhanced diagnosis testing value than with several widely used soft tissue labeling methods.

1 Introduction

Image-guided diagnosis of brain disease calls for accurate morphometry algorithms, e.g., in order to detect focal atrophy patterns relating to early-stage progression of particular forms of dementia. To date, widely used brain morphometry packages rest upon discrete Markov random field (MRF) image segmentation models [1, 2] that ignore, or do not fully account for *partial voluming*, leading to potentially inaccurate estimation of tissue volumes. Although several partial volume (PV) estimation methods have been proposed in the literature from the early 90’s [3–8], none of them seems to be in common use.

One difficulty with PV estimation from a single real-valued image is the necessity to incorporate strong prior knowledge. As already observed in [3], for a number K of tissues, a maximum likelihood approach leads to solving for each voxel one equation with $K - 1$ unknown concentrations, which has multiple solutions when $K > 2$. This is easily understood by considering an example of T1-weighted brain MR image where the mean intensity values of cerebrospinal fluid (CSF), gray matter (GM) and white matter (WM) are, say, 50, 150, and 250, respectively. Any voxel in the brain with intensity 150 could contain either

** Data used in preparation of this article were obtained from the Alzheimer’s Disease Neuroimaging Initiative (ADNI) database (adni.loni.ucla.edu). As such, the investigators within the ADNI contributed to the design and implementation of ADNI and/or provided data but did not participate in analysis or writing of this report. A complete listing of ADNI investigators can be found at: http://adni.loni.ucla.edu/wp-content/uploads/how_to_apply/ADNI_Acknowledgement_List.pdf.

100% GM, or 50% CSF and 50% WM, or any concentrations of CSF, GM and WM that match an average intensity of 150. A possibility to disambiguate the problem is to use multichannel MR images [3, 9], which have the effect to increase the number of constraints on the unknown concentrations but are only available from specific clinical protocols.

There exist soft labeling methods that compute tissue weights which are sometimes incorrectly interpreted as concentrations. For instance, the variational expectation-maximization (VEM) algorithm for discrete MRF models [1, 10] computes posterior membership probabilities under assuming a single tissue per voxel. Tissue weights output by the fuzzy C-mean [11, 12] or random walker [13] algorithms have no clear relation to PV.

Some authors have proposed to estimate PV in the conventional discrete segmentation framework by including labels that represent mixed tissue classes modeled by intensity distributions that may reflect PV effects physically [14], or be computationally more convenient Gaussian distributions [15, 2]. Such approaches have the potential to pinpoint voxels affected by strong PV, but are expected to underestimate PV overall. Another strategy that stays within the framework of discrete MRF models is to perform tissue classification at super-resolution, hence completing a more ambitious task than estimating voxelwise tissue concentrations. This was tackled in [7] using a Monte Carlo variant of the VEM algorithm, which appears to require heavy computation and memory load.

2 A regularized tissue concentration model

2.1 Bayesian formulation

We propose to revisit methods that rely on *continuous* MRFs and formulate tissue concentration estimation as a Bayesian maximum a posteriori (MAP) problem following [3, 4, 6, 8]. Let Y denote an input MR image previously submitted to various artifact corrections and skull stripping. We assume the following image appearance model within the intra-cranial mask:

$$y_i = \boldsymbol{\mu}^\top \mathbf{q}_i + \varepsilon_i, \quad \varepsilon_i \sim N(0, \sigma), \quad (1)$$

where y_i denotes intensity at voxel with index i , \mathbf{q}_i is the associated tissue concentration vector, $\boldsymbol{\mu}$ is the 3-dimensional vector of tissue means corresponding to CSF, GM and WM, respectively, and σ is the noise standard deviation. The assumption of Gaussian noise with constant σ across tissues is justified under large SNR for amplitude images, and more generally for phase array sum-of-squares images, as a first-order approximation to the noncentral chi distributed noise derived from imaging physics [16, 17]. Note that, in discrete labeling models, it is common to assume tissue-dependent variances to account for both acquisition noise and PV effects, however PV effects are modeled deterministically here.

Unknown in (1) are the concentration map $Q = (\mathbf{q}_1, \mathbf{q}_2, \dots)$ and the global parameters $(\boldsymbol{\mu}, \sigma)$. A maximum likelihood estimation approach would lead to

minimize w.r.t. Q , $\boldsymbol{\mu}$ and σ :

$$-2 \log P(Y|Q, \boldsymbol{\mu}, \sigma) = n \log 2\pi\sigma^2 + \frac{1}{\sigma^2} \sum_i (y_i - \boldsymbol{\mu}^\top \mathbf{q}_i)^2, \quad (2)$$

where n is the total number of voxels. As mentioned in the introduction, this is an ill-posed problem. Consider for instance a voxel where the intensity y_i is within the extremal values of $\boldsymbol{\mu}$; we then have an infinity of \mathbf{q}_i 's for which $y_i = \boldsymbol{\mu}^\top \mathbf{q}_i$, hence minimizing $(y_i - \boldsymbol{\mu}^\top \mathbf{q}_i)^2$. Moreover, it can be seen that by choosing Q in this fashion, the likelihood becomes infinite for $\sigma = 0$ and $\boldsymbol{\mu}$ with extremal values $\mu_1 = -\infty$ and $\mu_3 = +\infty$. Therefore, maximum likelihood estimators of Q , $\boldsymbol{\mu}$ and σ are both non-unique and physically implausible.

In order to regularize the problem, we add a prior under the form $P(Q, \boldsymbol{\mu}, \sigma) = P(Q)P(\boldsymbol{\mu}, \sigma)$ that expresses three types of knowledge: 1) voxels with mild PV are more frequent than with strong PV; 2) tissue concentration maps are spatially smooth; and 3) mean tissue intensities are bounded. The first two constraints are achieved by:

$$P(Q) \propto e^{-\frac{1}{2} \sum_i \mathbf{q}_i^\top V_\alpha \mathbf{q}_i - \frac{\beta}{2} \sum_{i,j \in \mathcal{N}_i} \|\mathbf{q}_i - \mathbf{q}_j\|^2}, \quad \text{with } V_\alpha = \begin{pmatrix} 0 & \alpha_1 & \alpha_2 \\ \alpha_1 & 0 & \alpha_3 \\ \alpha_2 & \alpha_3 & 0 \end{pmatrix}, \quad (3)$$

where V_α is a symmetric hollow matrix parametrized by a fixed vector $\boldsymbol{\alpha} \succeq 0$, $\beta > 0$ is another fixed parameter and \mathcal{N}_i stands for the set of neighbors of voxel i in the intra-cranial mask according to a 6-topology in this work. In the limit where $\min \boldsymbol{\alpha} \rightarrow \infty$, each term $\mathbf{q}_i^\top V_\alpha \mathbf{q}_i$ becomes infinite unless \mathbf{q}_i concentrates on a single tissue, therefore the prior imposes a hard labeling constraint. The further term weighted by β is a classical interaction potential also used in [3, 4, 8] to favor smooth concentration maps.

As for the global parameters, we choose a prior that prevents an implausibly large gap between mean tissue intensities,

$$P(\boldsymbol{\mu}, \sigma) \propto e^{-\gamma \frac{n}{2\sigma^2} \|\boldsymbol{\mu} - m\mathbf{1}\|^2}, \quad (4)$$

where $\gamma > 0$ and m are additional real-valued parameters. In our implementation, γ is fixed similarly to $\boldsymbol{\alpha}$ and β . Combining the likelihood (2) with the priors (3) and (4), we see that the MAP problem boils down to minimizing the following cost function:

$$\begin{aligned} C(Q, \boldsymbol{\mu}, \sigma, m) = & n \log 2\pi\sigma^2 + \frac{1}{\sigma^2} \sum_i (y_i - \boldsymbol{\mu}^\top \mathbf{q}_i)^2 + \sum_i \mathbf{q}_i^\top V_\alpha \mathbf{q}_i \\ & + \beta \sum_{i,j \in \mathcal{N}_j} \|\mathbf{q}_i - \mathbf{q}_j\|^2 + \gamma \frac{n}{2\sigma^2} \|\boldsymbol{\mu} - m\mathbf{1}\|^2. \end{aligned} \quad (5)$$

2.2 MAP tracking algorithm

It is natural to minimize (5) iteratively by alternating minimization along Q , $(\boldsymbol{\mu}, \sigma)$ and m , yielding three steps:

Step 1. Finding the optimal concentration map Q at fixed $(\boldsymbol{\mu}, \sigma)$ and m amounts to a quadratic optimization problem subject to linear constraints since Q is restricted to the multidimensional simplex, i.e., $\forall i, \mathbf{q}_i \succeq \mathbf{0}$ and $\mathbf{q}_i^\top \mathbf{1} = 1$. This is effectively done by looping over voxels in arbitrary order and solving for each \mathbf{q}_i with all other concentrations held fixed, yielding the following system:

$$\left(\frac{1}{\sigma^2} \boldsymbol{\mu} \boldsymbol{\mu}^\top + V_{\boldsymbol{\alpha}} + 2\beta n_i \mathbf{I} \right) \mathbf{q}_i - \frac{y_i}{\sigma^2} \boldsymbol{\mu} - 2\beta \sum_j \mathbf{q}_j + \lambda \mathbf{1} + \boldsymbol{\nu} = \mathbf{0},$$

where $n_i = \#\mathcal{N}_i \leq 6$ is the number of grid neighbors of voxel i , \mathbf{I} is the 3×3 identity matrix, and $(\lambda, \boldsymbol{\nu})$ are Karush-Kuhn-Tucker multipliers satisfying $\boldsymbol{\nu} \succeq \mathbf{0}$ and $\boldsymbol{\nu} \odot \mathbf{q}_i = \mathbf{0}$ that are determined using an active set algorithm [18].

Step 2. Compute the optimal $(\boldsymbol{\mu}, \sigma)$ at fixed Q and m , yielding:

$$\hat{\boldsymbol{\mu}} = \left(n\gamma \mathbf{I} + \sum_i \mathbf{q}_i \mathbf{q}_i^\top \right)^{-1} \left(n\gamma m + \sum_i y_i \mathbf{q}_i \right), \quad \hat{\sigma}^2 = \gamma \|\hat{\boldsymbol{\mu}} - m\mathbf{1}\|^2 + \frac{1}{n} \sum_i (y_i - \hat{\boldsymbol{\mu}}^\top \mathbf{q}_i)^2.$$

Step 3. Compute the optimal m at fixed Q and $(\boldsymbol{\mu}, \sigma)$: $\hat{m} = \boldsymbol{\mu}^\top \mathbf{1} / 3$.

The algorithm is initialized with uniform concentrations, i.e. $\forall i, \mathbf{q}_i = \mathbf{1}/3$, $\boldsymbol{\mu}$ as the three main histogram modes detected using scale-space analysis [19], and a tiny deviation $\sigma = 10^{-5}$ to ensure that the likelihood term predominates in early iterations. Each iteration requires about 5 seconds using C/Python code for a typical brain MR image on a standard single processor, which could probably be cut down by further code optimization for Step 1.

The algorithm involves fixed parameters $\boldsymbol{\alpha}$, β and γ that were tuned using a BrainWeb simulated T1 image [20] so as to minimize the Hellinger distance w.r.t. the fuzzy tissue volumes provided by BrainWeb, yielding:

$$\boldsymbol{\alpha} = (10.5, 29486, 7)^\top, \quad \beta = 1.2, \quad \gamma = 0.005.$$

Note that because α_2 turned out very large, the algorithm optimized in this manner practically proscribes tissue mixing involving both CSF and WM. This helps PV estimation in most brain areas but also creates a systematic artefactual ‘‘GM rim’’ around the ventricles, as seen in Figure 1, which could be avoided using spatially varying priors.

2.3 Comparison with other methods

Our MAP formulation (5) generalizes some previously proposed PV estimation algorithms. The case $\boldsymbol{\alpha} = \mathbf{0}$ and $\gamma = 0$ was studied in [3, 4, 8]. The algorithm proposed in [6] corresponds to choosing a uniform $\boldsymbol{\alpha} = (\alpha, \alpha, \alpha)^\top$ and setting $\beta = \frac{1}{2}\alpha$ and $\gamma = 0$. We observed from visual inspection that these special cases tend to massively overestimate PV on both BrainWeb and real data. Moreover, the γ parameter plays an essential role as it enables estimating intensity parameters $\boldsymbol{\mu}$ and σ along with tissue concentrations, preventing convergence towards an

absurd solution ($\mu_1 = -\infty$, $\mu_3 = +\infty$ and $\sigma = 0$), an issue that was overlooked in the above cited references.

Another related method, hereafter referred to as the Shattuck/Bach (SB) method [14, 15], relies on labeling voxels according to, e.g., 5 classes that represent pure CSF, GM and WM as well as mixed CSF/GM and GM/WM. This is done in [15] using a VEM algorithm that outputs membership posterior probability maps that are then converted into tissue concentrations using linear fractional content estimation based on adjacent pure tissue intensity means. Figure 1 illustrates the quantization effect produced by this approach compared to the proposed algorithm.

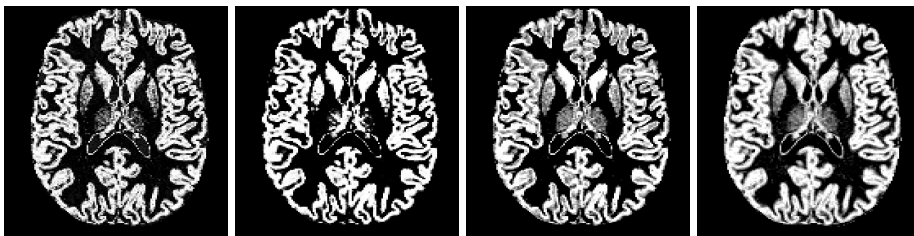


Fig. 1. Gray matter maps estimated from different methods for real data. From left to right, fuzzy C-mean, 3-class VEM, SB method, proposed MAP algorithm.

3 Experiments

We evaluated several tissue labeling methods on a *standardized analysis set* [21] from the Alzheimer’s Disease (AD) Neuroimaging Initiative (ADNI, adni.loni.ucla.edu) consisting of T1-weighted MR scans with approximately 1 mm^3 voxel size, from different 1.5T and 3T acquisition systems. The set comprises 818 subjects, including 229 diagnosed as normal (NL), 401 as mild cognitively impaired (MCI), and 188 as AD. For each subject, we used by default the 1.5T screening scan, or the 3T baseline scan when available (as is the case for 151 subjects), corrected for gradient distortion, B1 inhomogeneity and bias field, as provided by ADNI. All images were further skull-stripped using diffeomorphic registration [22] with an in-house brain MR template, and a crude hippocampus segmentation was performed similarly using a hippocampus mask drawn on the template by a neurologist.

For each ADNI case, we estimated both the global brain tissue ratio (BTR) and the normalized hippocampus volume (NHV) using tissue concentration or pseudo-concentration maps output by four different algorithms: the proposed PV estimation algorithm, the fuzzy C-mean algorithm [11, 12], the VEM algorithm using a conventional 3-class Gaussian mixture model [1, 10], and the SB method using a 5-class model [15], see Section 2.3. The BTR was defined as $\text{BTR} =$

Marker	Comparison	MAP method		SB method		3-class VEM		Fuzzy C-mean	
		LR ₊	LR ₋						
BTR	AD vs NL	2.177	0.278	2.052	0.282	1.994	0.301	1.994	0.351
	MCI vs NL	1.661	0.394	1.593	0.407	1.494	0.385	1.548	0.419
	AD vs MCI	1.479	0.671	1.468	0.679	1.431	0.675	1.463	0.668
NHV	AD vs NL	3.365	0.165	3.147	0.169	2.865	0.170	3.022	0.160
	MCI vs NL	2.008	0.301	1.911	0.309	1.723	0.347	1.891	0.315
	AD vs MCI	1.803	0.611	1.746	0.621	1.565	0.664	1.733	0.628

Table 1. Cross-validated positive and negative likelihood ratios for linear classifiers using respectively age+BTR (top rows) and age+NHV (bottom rows) as features. The largest LR₊ and smallest LR₋ are shown in bold for each comparison.

$(vol_{GM} + vol_{WM})/vol_{TIV}$, where vol_{GM} and vol_{WM} are the global GM and WM volumes, respectively, and $vol_{TIV} = vol_{CSF} + vol_{GM} + vol_{WM}$ is the total intracranial volume. The NHV was defined as $NHV = (vol_{GM}^* + vol_{WM}^*)/vol_{TIV}$, where vol_{GM}^* and vol_{WM}^* were the estimated GM and WM volumes within the crude hippocampus mask.

Both the 3-class and SB methods involve a Markov/Potts ‘beta’ regularization parameter that was optimized using the same BrainWeb matching criterion as for the proposed PV algorithm (see Section 2.2), respectively yielding $\beta = 0.2$ and $\beta = 0.4$ (note that the MAP algorithm was the one achieving the smallest minimal Hellinger distance w.r.t. the BrainWeb fuzzy maps). All algorithms were initialized by the same tissue means found by histogram mode detection [19] and tiny within-class standard deviations 10^{-5} , and run until variations on tissue maps were as small as for the MAP algorithm after 25 iterations. For the SB method, initial CSF/GM and GM/WM means were computed by averaging adjacent histogram modes.

Two-dimensional linear classifiers using respectively age+BTR and age+NHV as features were implemented for each soft labeling method and cross-validated using a standard leave-one-out procedure in three distinct classification scenarios: AD vs NL, MCI vs NL, and AD vs MCI. Table 1 reports obtained positive and negative likelihood ratios, $LR_+ = \text{sensitivity}/(1 - \text{specificity})$ and $LR_- = (1 - \text{sensitivity})/\text{specificity}$. These values represent post-test disease odds corresponding to even pre-test odds, respectively given a positive or negative test. The proposed PV estimation algorithm is seen to achieve the largest LR_+ and nearly smallest LR_- in all cases, suggesting its potential to improve diagnostic testing value over conventional atrophy detection methods. McNemar tests for classifier comparison [23] were however short of significance in most cases, indicating that the improvement is mild on the simple classification strategies considered here.

4 Conclusion

This work contributes to demonstrate the feasibility of PV estimation from conventional T1-weighted images without resorting to additional image acquisitions.

We have extended the “mixel” model originally proposed by Choi *et al* [3] and further developed in [4, 8, 6] so as to alleviate two important drawbacks. First, previous “mixel” models do not enable simultaneous updating of tissue concentration maps and global intensity parameters. Second, they tend to overestimate PV effects as they do not include a tissue homogeneity prior, or use too weak a prior [6].

Our disease classification experiments indicate that the proposed PV estimation algorithm enables more accurate detection of AD and MCI from simple volume biomarkers than conventional brain morphometry methods, thereby confirming the benefit of PV modeling for image-guided diagnosis. While the improvement is mild for the single-biomarker classifiers tested in this work, we anticipate that stronger effects could be seen in multi-dimensional classification using highly localized biomarkers (e.g. voxelwise concentrations), where accurate PV estimation would seem important to detect subtle atrophy patterns.

Extensions of the presented method using atlas-based priors may be needed to correct for systematic errors at the CSF/WM interface, as shown in Figure 1, as well as to tackle estimation of abnormal WM, which is frequent in elderly subjects and is characterized by a drop in WM intensity that makes it appear like GM. The use of atlas-based priors in image-guided diagnosis is however an open research topic as recent work suggests that conventional atlas-based tissue classification methods may lead to reduced population discrimination [24].

References

1. Van Leemput, K., Maes, F., Vandermeulen, D., Suetens, P.: Automated model-based tissue classification of MR images of the brain. *IEEE Transactions on Medical Imaging* **18**(10) (1999) 897–908
2. Ashburner, J., Friston, K.: Unified segmentation. *NeuroImage* **26**(3) (2005) 839–851
3. Choi, H.S., Haynor, D.R., Kim, Y.: Partial Volume Tissue Classification of Multichannel Magnetic Resonance Images – A Mixel Model. *IEEE Transactions on Medical Imaging* **10**(3) (1991) 395–407
4. Nocera, L., Gee, J.C.: Robust partial volume tissue classification of cerebral MRI scans. In: *SPIE Medical Imaging*. Volume 3034., SPIE (1997) 312–322
5. Laidlaw, D.H., Fleischer, K.W., Barr, A.H.: Partial-volume Bayesian classification of material mixtures in MR volume data using voxel histograms. *IEEE Transactions on Medical Imaging* **17**(1) (1998) 74–86
6. Pham, D.L., Prince, J.L.: Unsupervised partial volume estimation in single-channel image data. In: *IEEE Workshop on Mathematical Methods in Biomedical Image Analysis (MMBIA)*, IEEE (2000) 170–177
7. Van Leemput, K., Maes, F., Vandermeulen, D., Suetens, P.: A Unifying Framework for Partial Volume Segmentation of Brain MR Images. *IEEE Transactions on Medical Imaging* **22**(1) (2003) 105–119
8. Liang, Z., Wang, S.: An EM Approach to MAP Solution of Segmenting Tissue Mixtures: A Numerical Analysis. *IEEE Transactions on Medical Imaging* **28**(2) (2009) 297–310

9. Duché, Q., Acosta, O., Gambarota, G., Merlet, I., Salvado, O., Saint-Jalmes, H.: Bi-exponential magnetic resonance signal model for partial volume computation. In: Medical Image Computing And Computer-Assisted Intervention (MICCAI). Volume 7510 of LNCS., Nice, France, Springer Verlag (October 2012) 231–238
10. Roche, A., Ribes, D., Bach-Cuadra, M., Krueger, G.: On the Convergence of EM-Like Algorithms for Image Segmentation using Markov Random Fields. *Medical Image Analysis* **15**(6) (2011) 830–839
11. Brandt, M.E., Bohant, T.P., Kramer, L.A., Fletcher, J.M.: Estimation of CSF, white and gray matter volumes in hydrocephalic children using fuzzy clustering of MR images. *Computerized Medical Imaging and Graphics* **18**(1) (1994) 25–34
12. Pham, D.L., Prince, J.L.: Adaptive fuzzy segmentation of magnetic resonance images. *IEEE Transactions on Medical Imaging* **18**(9) (1999) 737–752
13. Grady, L.: Random Walks for Image Segmentation. *IEEE Transactions on Pattern Analysis and Machine Intelligence* **28**(11) (2006) 1768–1783
14. Shattuck, D., Sandor-Leahy, S., Schaper, K., Rottenberg, D., Leahy, R.: Magnetic resonance image tissue classification using a partial volume model. *NeuroImage* **13**(5) (2001) 856–876
15. Bach Cuadra, M., Cammoun, L., Butz, T., Cuisenaire, O., Thiran, J.P.: Comparison and validation of tissue modelization and statistical classification methods in T1-weighted MR brain images. *IEEE Transactions on Medical Imaging* **24**(12) (2005) 1548–1565
16. Gudbjartsson, H., Patz, S.: The Rician Distribution of Noisy MRI Data. *Magnetic Resonance in Medicine* **34**(6) (1995) 910–914
17. Larsson, E.G., Erdogmus, D., Yan, R., Principe, J.C., Fitzsimmons, J.R.: SNR-optimality of sum-of-squares reconstruction for phased-array magnetic resonance imaging. *Journal of Magnetic Resonance* **163** (2003) 121–123
18. Nocedal, J., Wright, S.: Numerical Optimization. Springer, New York (1999)
19. Dauguet, J., Mangin, J.F., Delzescaux, T., Frouin, V.: Robust inter-slice intensity normalization using histogram scale-space analysis. In: Medical Image Computing And Computer-Assisted Intervention (MICCAI). LNCS, St Malo, France, Springer Verlag (September 2004) 242–249
20. Kwan, R.S., Evans, A., Pike, G.: MRI simulation-based evaluation of image-processing and classification methods. *IEEE Transactions on Medical Imaging* **18**(11) (1999) 1085–1097
21. Wyman, B., Harvey, D., Crawford, K., Bernstein, M., Carmichael, O., Cole, P., Crane, P., Decarli, C., Fox, N., Gunter, J., Hill, D., Killiany, R., Pachai, C., Schwarz, A., Schuff, N., Senjem, M., Suhy, J., Thompson, P., Weiner, M., Jack, C., the Alzheimer’s Disease Neuroimaging Initiative: Standardization of analysis sets for reporting results from ADNI MRI data. *Alzheimer’s & Dementia* (2012) In Press.
22. Chéfd’hotel, C., Hermosillo, G., Faugeras, O.: Flows of diffeomorphisms for multi-modal image registration. In: Proc. IEEE International Symposium on Biomedical Imaging. (2002) 753–756
23. Bostanci, B., Bostanci, E.: An evaluation of classification algorithms using Mc Nemar’s test. In: Proceedings of Seventh International Conference on Bio-Inspired Computing: Theories and Applications (BIC-TA 2012), Springer (2013) 15–26
24. Ribes, D., Mortamet, B., Bach-Cuadra, M., Jack, C., Meuli, R., Krueger, G., Roche, A.: Comparison of tissue classification models for automatic brain MR segmentation. In: International Society for Magnetic Resonance in Medicine (ISMRM’11), Montreal, Canada (2011)